



Comparison of low-cycle fatigue properties of two kinds of high energy beam welded joints of TC4 alloy

Jian LONG¹, Lin-jie ZHANG¹, Lei ZHU¹, Li-xu ZHANG², Jun WU², Ming-xiang ZHUANG³

1. State Key Laboratory for Mechanical Behavior of Materials, Xi'an Jiaotong University, Xi'an 710049, China;
2. Xi'an Aerospace Power Machine Factory Co., Ltd., Xi'an 710025, China;
3. AVIC Xi'an Aircraft Industry (Group) Company Ltd., Xi'an 710089, China

Received 21 April 2022; accepted 20 September 2022

Abstract: The low-cycle fatigue properties of 30 mm Ti6Al4V titanium alloy joints welded by vacuum electron beam welding and laser wobble welding with filler wire were compared. The test results show that the low-cycle fatigue performance of the electron beam welding joint is close to that of the base metal, while the low-cycle fatigue performance of the laser wobble welding with a filler wire joint is clearly inferior to that of the electron beam welding joint and base metal. An examination of the microhardness of the base metal, heat-affected zones and weld area of the two joints found that the microhardness of the weld area of the electron beam welding joint is close to that of the base metal, but is lower than that of the heat-affected zones on both sides. The weld area of the laser wobble welding with the filler wire joint is significantly weakened.

Key words: Ti6Al4V titanium alloy; microstructure; microhardness; low-cycle fatigue

1 Introduction

Due to advantages, such as high energy density, low heat input, a large depth-to-width of the weld metal (WM), small welding deformation, and good stability, vacuum electron beam welding (EBW) technology has been widely used in the aerospace industry [1,2]. This technology is beneficial to the integrated manufacturing of large aerospace structural parts. Titanium (Ti) and its alloy are highly suitable for the lightweight aviation manufacturing because of their advantages such as low density, high specific strength, good corrosion resistance, high toughness, and fatigue resistance [3,4]. Furthermore, many parts of advanced aircrafts and engines are manufactured using Ti alloy, and the proportion of Ti alloy in aircraft has even become an important indicator for measuring the level of aircraft

advancement and developments. However, Ti alloys are relatively chemically active and easily react with impurity gases, such as oxygen, hydrogen and water vapor during welding, resulting in the weakened performance of the workpieces. High-energy beams used in welding include plasma arcs, electron beams, and laser beams, with different advantages and disadvantages for each technology. The advantage of laser wobble welding with filler wire (LWFW) is that welding can be performed in an atmospheric environment; however, defects in sidewalls and interlayers can easily appear. EBW is advantageous in that the welding quality is outstanding in a vacuum chamber due to the unique advantages of the high-vacuum environment for EBW for the welding of Ti alloys [5,6]. However, EBW has limitation, most importantly that the size of the welding plate is limited. When the size of a component to be welded is larger than that of a

vacuum chamber for EBW, EBW can no longer be used. Similar to EBW, laser welding, as well as high-energy beam welding, has advantages, such as high energy density, a small heat-affected zone (HAZ), high welding speed and good welding quality, furthermore, it can be used in the atmospheric environment [7–9]. Therefore, compared to EBW, laser welding has better adaptability. Through single-pass and multi-layer LFWW, large and thick plates can be welded using a low-power laser; this method, not only retains the advantages of laser welding, but also is not limited by the dimensions of the components. Therefore, LFWW is expected to be a key welding technology in the future [10,11]. In recent years, many researchers have conducted studies on LFWW technology. SHI et al [12] revealed the relationship between single-pass welding parameters and geometrical shapes of the WM using a statistical modeling and established a mathematical model for the relationship between the input processing variables and the geometrical shapes of weld beads. The test results demonstrate that the optimized formula can be used to plan welding paths and realize the welding of high-strength steel with a thickness of 20 mm used for ships, showing well-fused sidewall and high-quality WM. By utilizing a 4 kW fiber laser, YU et al [13] welded Q235 low-carbon steel plates with a thickness of 17 mm using narrow-gap LFWW and studied the influence of the groove size on welding quality. The use of a relatively small root size of the groove was found not only to decrease the consumption of the filler wire, but also to reduce the left-right asymmetric deposition of the filler wire in the weld bead, thus improving the

fusion between the filler metal and the sidewall.

In conclusion, research on LFWW technology conducted around the world has mainly examined the welding process, welding deformation and defect control, while the fatigue performance of LFWW joints has not been explored. Some studies have shown that fatigue is a major problem affecting the safety and durability of modern aviation equipment. Fatigue can also lead to a substantial increase in maintenance cost; therefore, it has become a key problem that needs to be solved in the design of the structural integrity of aviation equipment [14]. This study compared the difference in the microstructures and low-cycle fatigue (LCF) performance of EBW and LFWW joints with the same thickness (30 mm), providing data supporting the application of these two welding technologies in aviation manufacturing.

2 Experimental

2.1 Materials and welding parameters

Ti6Al4V (TC4) alloy was used in this study and its chemical composition is listed in Table 1. Tables 2 and 3 present the welding parameters used for the EBW and LFWW joints, respectively. In this experiment, inert gas protection was used in the laser welding process. The welding shielding gas was argon (Ar), the gas flow rate was 10 L/min, and the gas purity was 99.99%. In the laser welding with filler wire experiment, the wire diameter was 1.0 mm, and its chemical composition was the same as that of the base metal (BM). The welding wire was placed at the center of the laser spot, and the laser-wire distance was 0 mm.

Table 1 Chemical composition of TC4 alloy (wt.%)

Al	V	Fe	C	N	H	O	Si	Ti
5.90	4.20	< 0.25	0.028	0.0042	0.0011	0.0395	< 0.026	Bal.

Table 2 EBW parameters

Voltage, U/kV	Focus current, I_f/mA	Speed, $v/(\text{mm}\cdot\text{s}^{-1})$	Beam current, I_b/mA	Scanning frequency/Hz	Scanning shape
60	2108	6	350	200	Circle

Table 3 LFWW parameters

Defocus, f/mm	Laser power, P/kW	Welding speed, $V/(\text{cm}\cdot\text{min}^{-1})$	Feeding speed, $V_f/(\text{m}\cdot\text{min}^{-1})$	Wobbling amplitude, a/mm	Wobbling frequency, T/Hz
58	3.8	30	3.12	3	100

2.2 Microstructure observation

The microstructures of the two joints were observed in three zones, namely the BM, HAZ and WM, using an FEI Verios460 field-emission scanning electron microscope (SEM). Keller's reagent (HF:HNO₃:H₂O=3:6:91) was used as a corrodent, and the corrosion lasted for approximately 15 s.

The electron backscatter diffraction (EBSD) tests were performed at an accelerating voltage of 15 kV, a working distance of approximately 20 mm, and a step size of 0.3 μm.

The microstructural morphologies of the BM and WM were observed using a JEM-2100 F high-resolution transmission electron microscope (TEM). Methanol sulfate solution with a concentration of 8% was used as the electrolyte.

2.3 Microhardness tests

The micro-Vickers hardness curve spans from the BM on the left side to the BM on the right side, with a dot interval of 0.5 mm. An HXD-1000TMC/LCD microhardness tester containing an automatic turret that can perform image analysis was used. The test force was 1.961 N and the load was maintained for 15 s.

2.4 LCF test

Figure 1 shows a schematic of the sampling of the joint fatigue specimens. It was obtained from the joint perpendicular to the weld axis, and the sample was located at the center of the joint thickness direction.

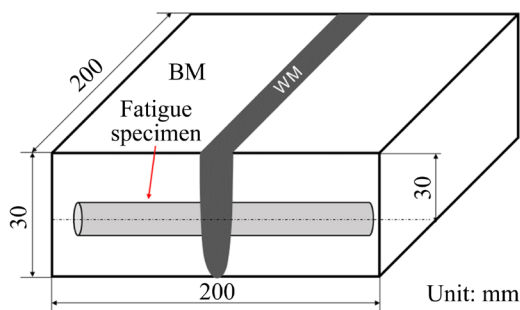


Fig. 1 Schematic diagram of sampling of fatigue specimens

The LCF test was conducted according to the test method for axial loading constant-amplitude low-cycle fatigue of metallic materials (GB/T 15248—2008) using an INSTRON-1341

instrument at room temperature in an atmospheric environment. Axial strain was controlled in the range from $\pm 0.5\%$ to $\pm 1.2\%$ and the strain ratio was -1 . The waveforms were symmetrical triangular waves with a strain rate of $0.4\%/s$. The gauge length of the extensometer used in this study was 12.5 mm. A 25% reduction of the maximum load was considered as the criterion for determining failure. The dimensions of the fatigue sample of BM are shown in Fig. 2. Figure 3 shows the schematic diagram of the dimensions of the fatigue samples of the EBW and LFW joints. The working section consisted of the BM, HAZ, and WM. The length of the test bar was 140 mm and the diameter of the clamped end was 12 mm. The working section had a diameter of 6 mm and a length of 30 mm. The WM was located at the center of the sample.

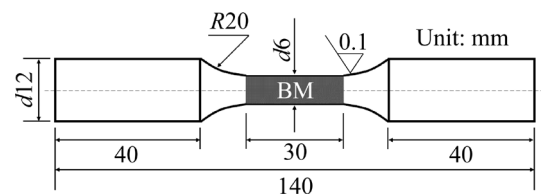


Fig. 2 Dimensions of fatigue sample of BM

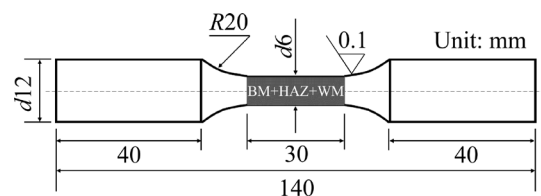


Fig. 3 Dimensions of fatigue sample of joint

2.5 Fracture surfaces

The fatigue fracture sample under the strain amplitude of $\pm 0.6\%$ was observed. Before observation, the fracture was ultrasonically cleaned in 99.7% ethanol solution for 30 min, and dried quickly thereafter. The fracture of the fatigue sample was observed with a SU3500 tungsten filament scanning electron microscope (SEM).

3 Results

3.1 Cross-sectional morphologies and microstructures of two joints

Figure 4 shows cross-sectional morphologies of the WM of the EBW and LFW joints with a thicknesses of 30 mm. Figure 4(a) illustrates the

cross-sectional morphology of the WM of the EBW joint of the test plates with a thickness of 30 mm. A backing plate with a thickness of 16 mm was used as the cushion. The upper part of the WM was wide and the size at the center tends to be stable. The widths of the WM and HAZ are 4–8 and 2–5 mm, respectively. Figure 4(b) shows the cross-sectional morphology of the LFWW joint with a thickness of 30 mm. A total of 15 passes were welded, in which the first pass was backing welding and the last pass was cosmetic welding. The WM was basically equal in width, in the range of 7–9 mm, and the width of the HAZ was 2–4 mm. The WM of the 30 mm-thick EBW joint was narrower than that of the LFWW joint, while the HAZ of the former was wider than that of the latter.

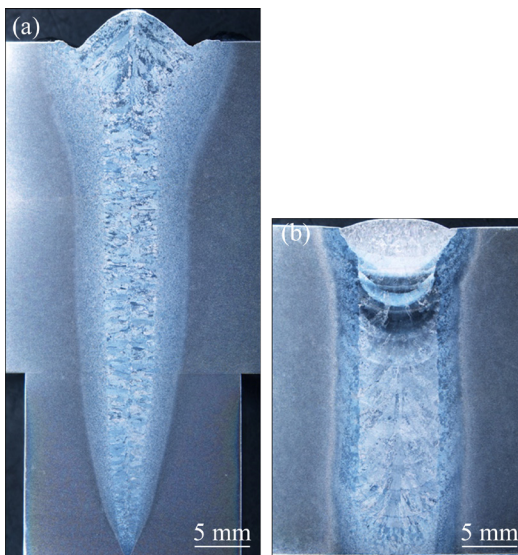


Fig. 4 Cross-sectional morphologies of WM of two joints: (a) EBW joint; (b) LFWW joint

3.2 Microstructure of two joints by SEM

Figure 5 shows the microstructures of each zone of the two joints by SEM. Figures 5(a) and (d) illustrate the microstructures of the BM of the EBW and LFWW joints, respectively. The BM of the two joints contains similar microstructures and belongs to the typical duplex microstructures, mainly including primary equiaxed α and β phases distributed along the α grain boundary. The HAZ is the transition zone between the BM and the WM, in which the primary equiaxed α phases do not completely transform, while some are transformed into lamellar α' phases and acicular martensite α' phases. Figures 5(b) and (e) show the micro-

structures in the HAZ of the two joints, in which there are a large number of lamellar α' phases arranged in a certain direction. The microstructures of the two joints mainly differ in the WM. The microstructures of the WM of the EBW and LFWW joints are shown in Figs. 5(c) and (f), respectively. The microstructures of the WM of the EBW joint mainly consist of lamellar α' phases along the grain boundary and acicular martensite α' phases. The locally magnified images of the microstructures of the WM show that lamellar α' phases are arranged in a certain direction. Previous studies show that such a microstructure is formed by slowing cooling from the β phase region where it is not either undeformed or slightly deformed after heating the alloy. If the alloy contains this microstructure, its plasticity and fatigue strength will be reduced; the origin of this effect requires further study. The microstructure of the WM of the LFWW joint mainly consists of lamellar α' phases and punctate β phases. Compared to the WM of the EBW joint, many fine β phases are present in the matrix of the WM of the LFWW joint. In the Ti alloy, β phases that are high-temperature phases have a body-centered cubic structure. When the materials are deformed under stress, β phases have more slip systems and are more prone to deformation than α phases with hexagonal close-packed crystal structures. This may be an important reason for the weakening of the WM of the LFWW joint.

3.3 Microhardness of two joints

Figure 6 displays the comparison of microhardnesses of the EBW and LFWW joints. As shown in the figure, the EBW and LFWW joints exhibit very similar microhardness. The main difference is shown in the WM. The average microhardness of the WM of the EBW joint is HV 329, while that of the LFWW joint is only HV 283, with a difference of HV 46. At the same time, the WM of LFWW joint is obviously weakened, and its average microhardness is HV 31 lower than that of BM.

3.4 Grain orientation of EBW and LFWW

Figure 7 shows the grain orientation of the two joints of electron beam welding (EBW) and laser welding with filler wire (LFWW). There are two

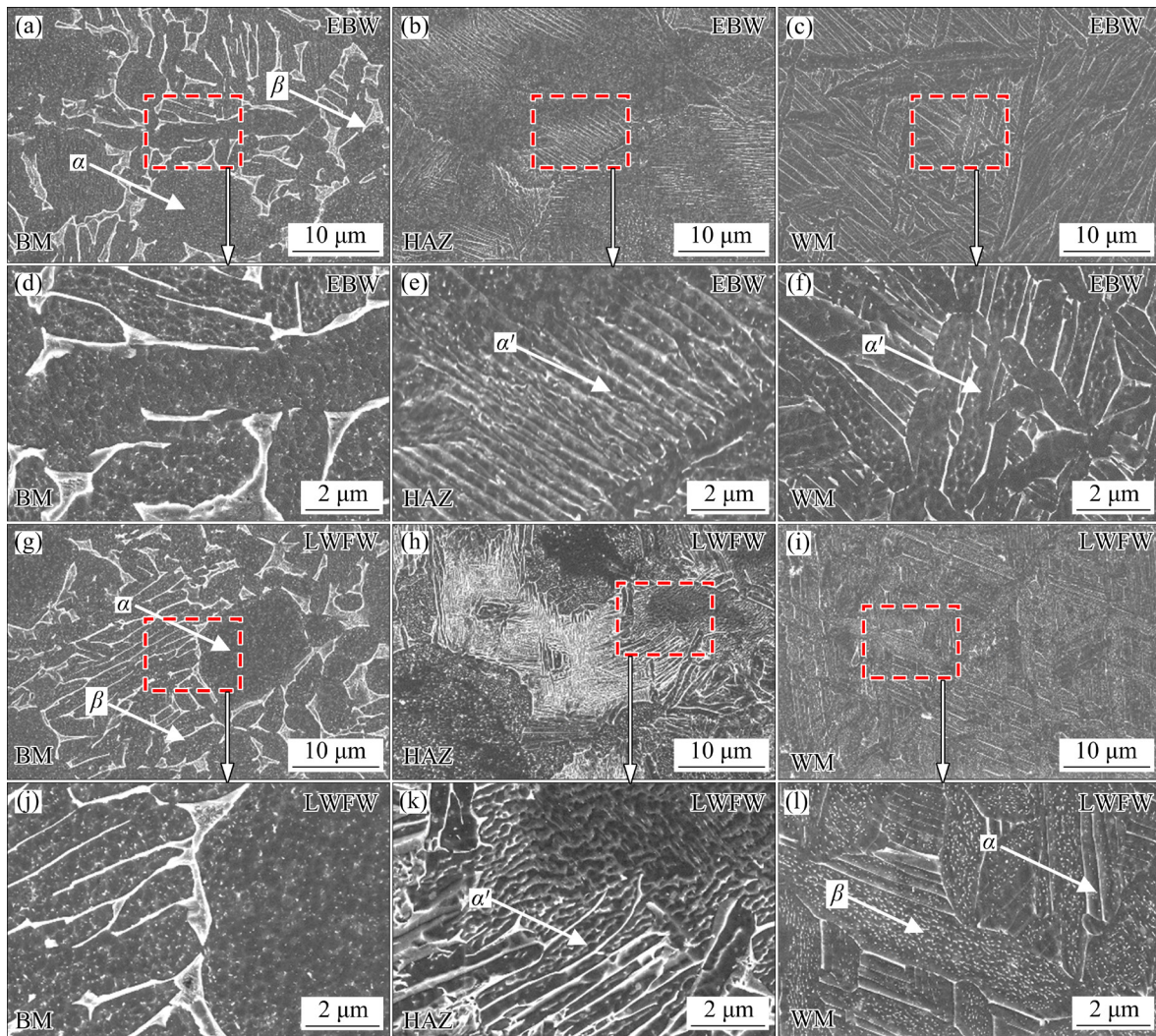


Fig. 5 SEM images of each zone of two joints

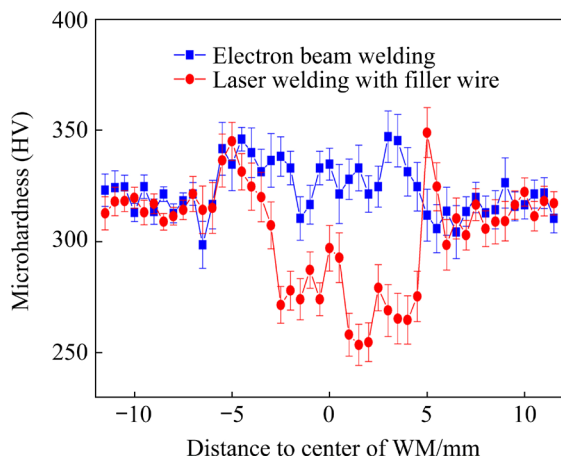


Fig. 6 Comparison of microhardnesses of each zone of EBW and LFWW joints with thickness of 30 mm

types of plastic deformation mechanisms in titanium alloys: slip and twinning, and twinning generally occurs in single crystal titanium and a few

titanium alloys. For the TC4 dual-phase titanium alloy, the Al element inhibits the twinning, so that deformation is mainly dominated by the dislocation movement of the α phase. The movement of dislocations occurs in the form of slip. In Fig. 7, the blue grains are the “hard orientation” grains with a lower Schmid factor, while the red grains are the “soft orientation” grains with a higher Schmid factor, indicating that these grains are more likely to slip and deform [15]. Figure 7(a) shows the grain orientation in the weld zone of the EBW joint, with fewer red grains. Figure 7(b) shows the grain orientation in the weld zone of LFWW joints, with more red grains.

It is observed that compared to the weld area of the EBW joint, the “soft-oriented” grains in the weld area of the LFWW joint are larger, and when the material is subjected to external loads and

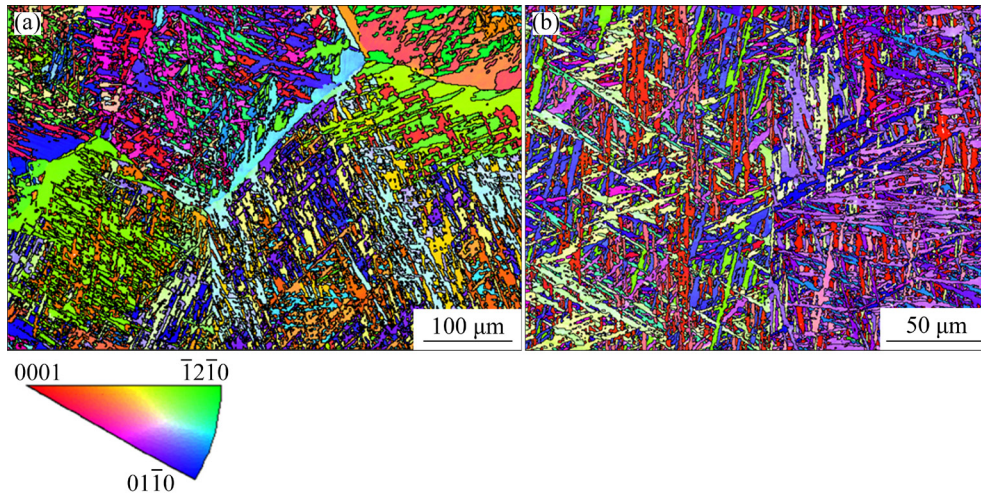


Fig. 7 Grain orientation of weld zone of EBW and LFWW joints: (a) EBW-WM; (b) LFWW-WM

deformed, the resistance to dislocation movement is lower, which is an important reason for the lower microhardness of the weld area of the LFWW joint compared to that of the EBW joint.

3.5 LCF performance of two joints

Table 4 lists the LCF test data for the BM and EBW and LFWW joints under different strain amplitudes. Based on the Zheng-Hirt formula, the LCF test data of the BM and the two joints are fitted to obtain the formula for the fatigue limit [16], as follows:

$$N_f = 94.577(\Delta\varepsilon_t - 0.49)^{-2} \tag{1}$$

$$N_f = 119.21(\Delta\varepsilon_t - 0.47)^{-2} \tag{2}$$

$$N_f = 32.71(\Delta\varepsilon_t - 0.41)^{-2} \tag{3}$$

where N_f and $\Delta\varepsilon_t$ represent the number of cycles and strain amplitude, respectively. Formulas (1)–(3) give the relationship between the strain amplitude and the number of cycles of the BM, EBW and LFWW joints of TC4 alloy. Under the test conditions, the fatigue limit of the BM in the LCF

Table 4 Number of cycles for LCF test of BM and EBW and LFWW joints under different strains

Joint	N_f				
	1.2%	1.0%	0.8%	0.6%	0.5%
BM	186	417	1721	6108	18927
	153	670	1775	5282	18526
EBW	255	581	1250	6354	15457
	168	518	1573	7190	17703
LFWW	61	156	306	3023	10236
	–	101	402	4032	8596

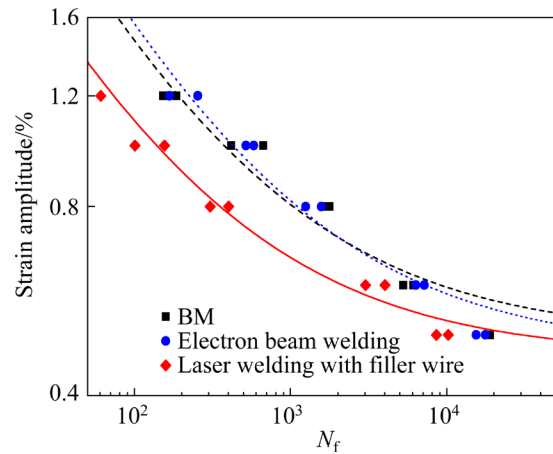


Fig. 8 ε – N_f curves of BM and EBW and LFWW joints of TC4 alloy in LCF test

test was 0.49%, while those of the EBW and LFWW joints were 0.47% and only 0.41%, respectively. Figure 8 shows the ε – N_f curves of the BM, EBW and LFWW joints of the TC4 alloy in the LCF test. According to Fig. 8, the LCF performance of the EBW joint is close to that of the BM, whereas the LCF performance of the LFWW joint is inferior to those of the EBW joint and BM.

4 Discussion

4.1 Fracture analysis of two joints in LCF test

Figure 9 shows the fracture morphologies of BM and the EBW and LFWW joints of the TC4 alloy in the LCF test. Figures 9(a)–(c) show the macro-morphologies of the fractures of the BM and the EBW and LFWW joints under LCF, respectively. Two main characteristic regions are observed,

among which a relatively flat fatigue region is shown on the right of the figure, and the rest are ultimate tensile fracture regions. Figures 9(d)–(f) show the crack initiation sources of the BM and the EBW and LFWW joints in the LCF test, respectively, and it is observed that fatigue cracks in the three samples initiate on the surfaces of the samples, showing a characteristic of multi-source initiation. Figures 9(g)–(i) show the fatigue crack growth regions in the BM and the EBW and LFWW joints, respectively. In these regions, clear fatigue striations are found, which are marks left by each cyclic loading on the samples [17,18]. Under cyclic tensile stress, the cracks begin to open, while the compressive stress loaded in the opposite direction makes the cracks unstable and form a groove at the

tip. Finally, under the maximum cyclic compressive stress, new cracks are formed and their lengths increase. Under such cycling, cracks continuously propagate forward. Unlike the BM and the EBW joint, secondary cracks appear in fatigue crack growth regions in the LFWW joint. Figures 9(j)–(l) display the ultimate tension fracture regions in the BM and the EBW and LFWW joints, respectively, where many dimples are found, showing good plasticity.

4.2 Fracture positions of two joints in LCF test

Figure 10 shows the fracture position of the EBW joint of the TC4 Ti alloy in the LCF test. According to the figure, the joint is fractured in the WM and the fatigue cracks initiate in the center of

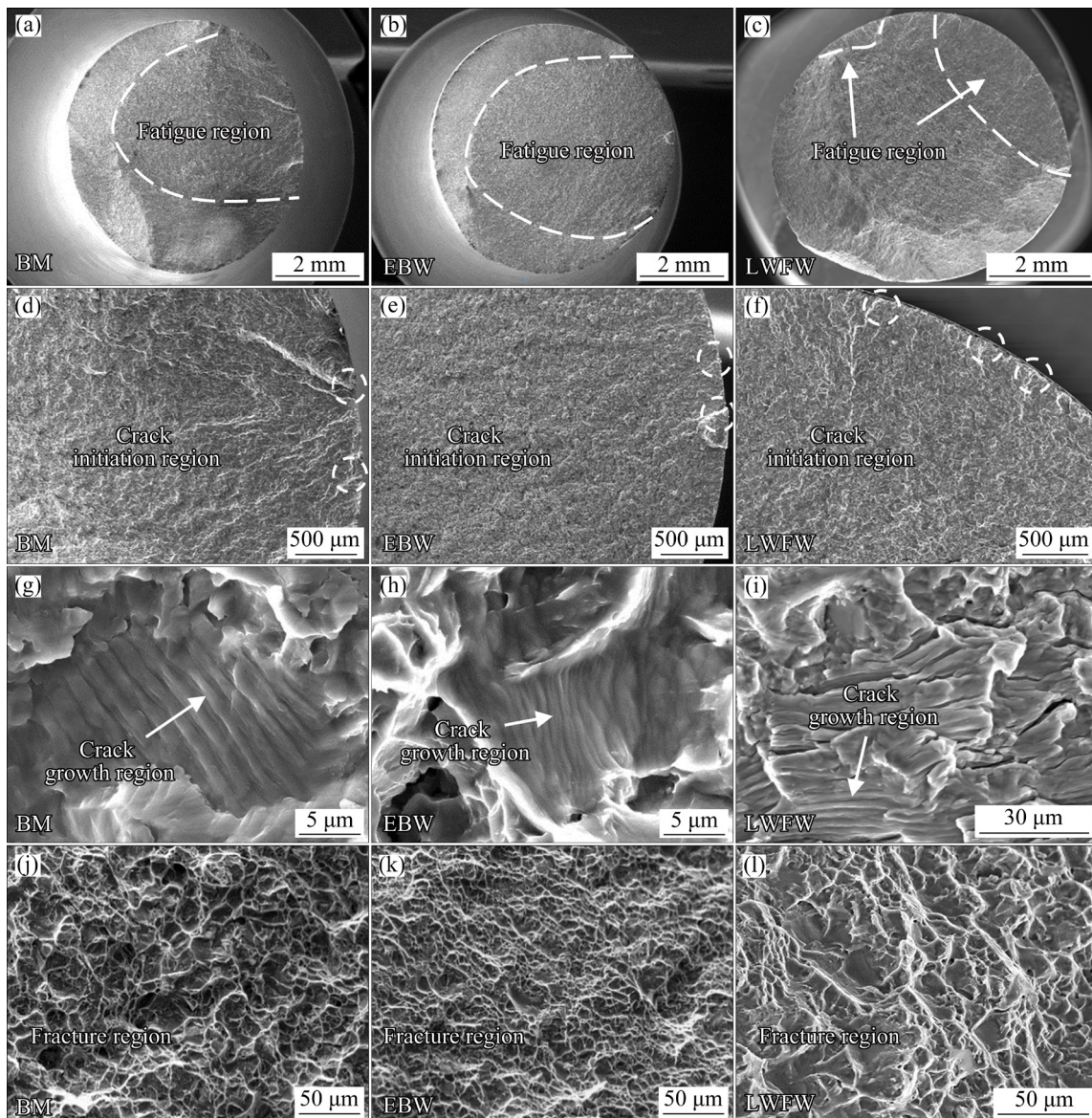


Fig. 9 Fracture morphologies of BM and EBW and LFWW joints of TC4 alloy in LCF test

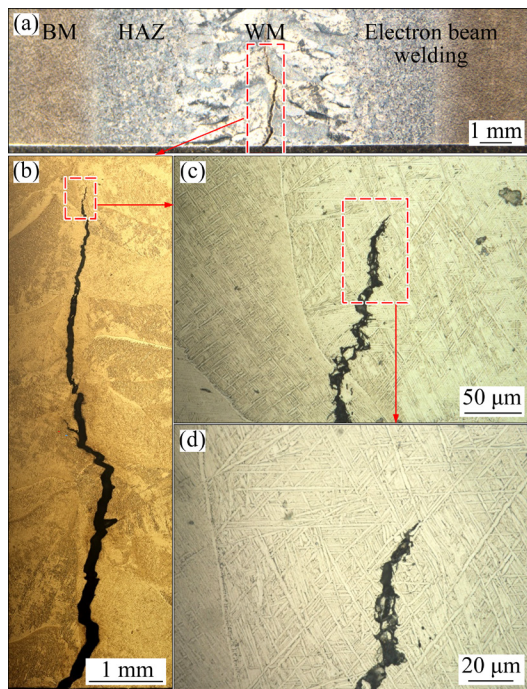


Fig. 10 Fracture position of EBW joint of TC4 Ti alloy in LCF test

the WM. The growth tips of the fatigue cracks tend to extend along the direction of the acicular martensite α' phases. This is because lower energy is required for the cracks to propagate along the acicular martensite α' phases than that for the cracks to pass through these phases. As shown in Fig. 6, the HAZs on both sides of the WM exhibit high microhardness: the average microhardness of the WM is HV 327, whereas those of the HAZs on the left and right sides of the WM are HV 346 and HV 347, respectively. During the fatigue test, stress may concentrate in the WM, which is an important factor contributing to the fracture of the LCF sample of the EBW joint in the WM.

Figure 11 shows the fracture position of the LFWW joint of the TC4 Ti alloy in the LCF test. It is observed from the figure that the joint is fractured in the WM and the position of crack initiation is close to the center of the WM. As shown in Fig. 6, the average micro-Vickers hardness of the BM and HAZ of the LFWW joint separately is HV 314 and HV 321, respectively, while that of the WM of the joint is only HV 283. There is a large microhardness gradient in the LFWW joint, and during the LCF test, stress concentration appears in the WM. The stress concentration exerts a particularly significant effect on the fatigue life of

materials, so that the LFWW joint is finally fractured in the WM during the LCF test. This is also an important reason for the inferior LCF performance of the LFWW joint compared to those of the EBW joint and BM.

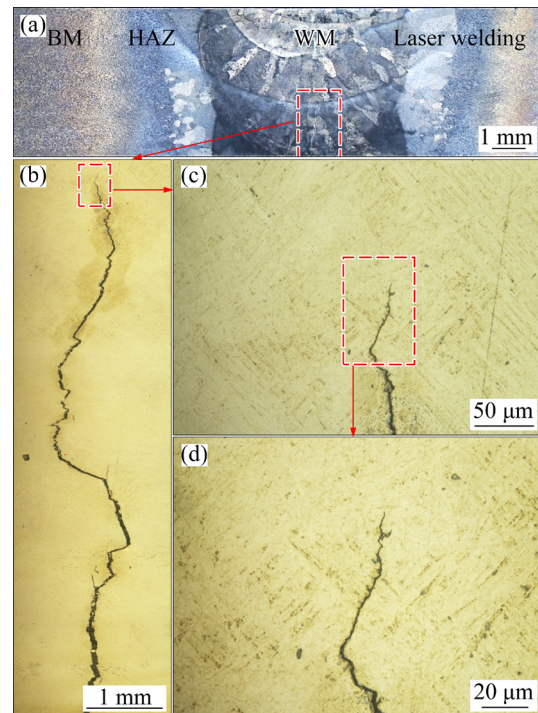


Fig. 11 Fracture position of LFWW joint in LCF test

4.3 Microstructure of each zone of two joints by TEM

Figure 12 shows the microstructures of BM, WM of EBW, and LFWW of the TC4 alloy by TEM. Figures 12(a) and (d) show the microstructure of the BM, which is mainly composed of a slate-like primary α phase and β phase distributed between the slats.

Figures 12(b) and (e) show the microstructure of the WM of EBW. A large amount of acicular martensite α' phases precipitated in the WM of the EBW. As the strengthening phase of titanium alloys, the acicular martensite α' phase requires more energy when the material is deformed under an external load, and the dislocation cuts through or bypasses the structure, increasing the movement resistance of the dislocation, which is conducive to improving the strength and hardness of the material. This is an important reason for the higher hardness of the WM of EBW compared to that of the BM. Meanwhile, numerous dislocation lines appeared in the α strip in the WM of the EBW joint. When the

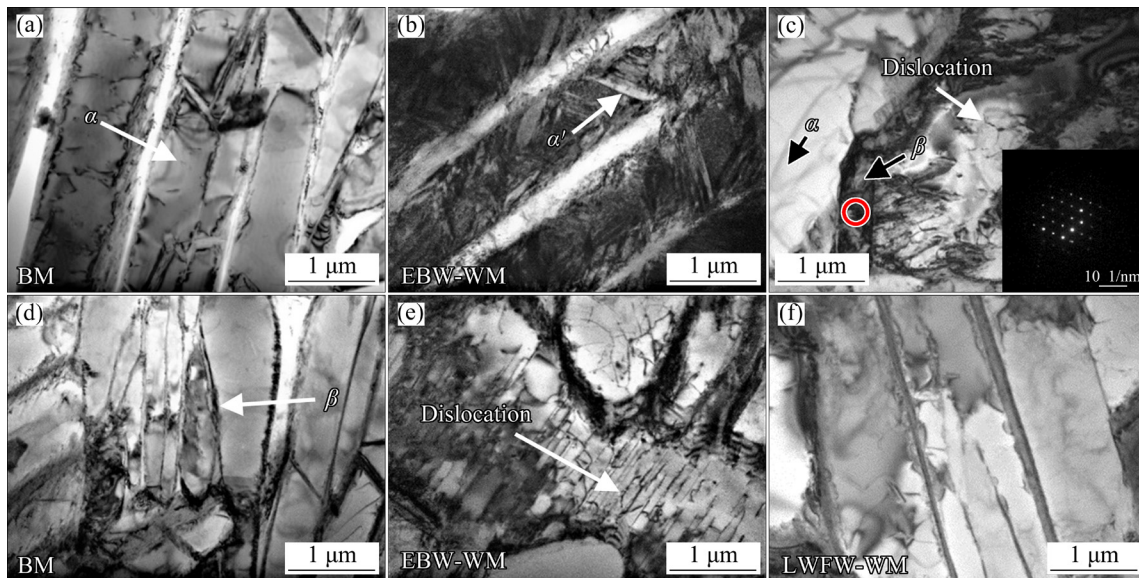


Fig. 12 Microstructures of BM, WM of EBW and LFWW of TC4 titanium alloy by TEM

material is deformed under an external load, these dislocation structures interact with the dislocation lines generated by deformation, increasing the movement resistance of the dislocation, which is also conducive to improving the strength and hardness of the material [19]. This is another important reason for the increased hardness of the weld zone of electron beam welding relative to that of the base metal.

Figure 12(f) shows the microstructure of the WM of LFWW. Compared to the BM, the α strip in the WM of the LFWW joint becomes wider. Simultaneously, the β phase at the grain boundary grew. The selected electron diffraction of this structure is shown in the right corner of Fig. 12(c), indicating a body-centered cubic structure. The β phase in titanium alloys is a high-temperature phase and has a body-centered cubic structure. When the material is subjected to external loads, more slip systems are present, and the resistance to dislocation movement is low [20]. This is an important reason for the decreased WM hardness of LFWW to that of the BM. Dislocation lines also appear in the WM of LFWW, but the dislocation density is clearly lower than that of EBW, which is also an important reason for the lower WM hardness of LFWW relative to that of EBW.

5 Conclusions

(1) Compared to the EBW joint, the LFWW joint shows worse LCF performance. The fatigue

limits of the LFWW and EBW joints in the LCF test are 0.41% and 0.47%, respectively.

(2) Compared to the EBW joint, a larger microhardness gradient is found in the LFWW joint. The average microhardness of the WM of the LFWW joint is HV 31 lower than that of the BM, whereas the microhardness of the WM of the EBW joint is close to that of the BM.

(3) In the LCF test, the EBW and LFWW joints are both fractured at the center of the WM.

(4) The microstructures of the WM of the EBW and LFWW joints are significantly different. SEM observations show that many punctate β phases appear in the WM of the LFWW joint, while there are few punctate β phases in the WM of the EBW joint.

Acknowledgments

This work was supported by the National Natural Science Foundation of China (No. 51775416), and National Thousand Talents Program of China (No. WQ2017610446). The authors would thank teachers at Instrument Analysis Center of Xi'an Jiaotong University for their assistance with SEM analysis. This work was also supported by the Project of Innovation Team of Xi'an Jiaotong University, China (No. XTR0118008).

References

- [1] XU Zhen-zhen, DONG Zhi-qiang, YU Zhao-hui, WANG Wen-ke, ZHANG Jian-xun. Relationships between micro-

- hardness, microstructure, and grain orientation in laser-welded joints with different welding speeds for Ti6Al4V titanium alloy [J]. Transactions of Nonferrous Metals Society of China, 2020, 30: 1277–1289.
- [2] LONG Jian, ZHANG Lin-jie, ZHANG Liang-liang, NING Jie, ZHUANG Ming-xiang, ZHANG Jian-xun, NA Suck-joo. Analysis of heterogeneity of fatigue properties of double-sided electron beam welded 140-mm thick TC4 titanium alloy joints [J]. International Journal of Fatigue, 2021, 142: 105942.
- [3] LIN Peng, XI Xian-zheng, ZHAO Wen-kai, YANG Rui-hong, LIN Fei, CUI Xiao-lei, LIU Gang. Microstructure and mechanical properties of Ti–6Al–4V/Ti–22Al–25Nb joint formed by diffusion bonding [J]. Transactions of Nonferrous Metals Society of China, 2021, 31: 1339–1349.
- [4] YANG Kun, HUANG Qi, ZHONG Bin, WANG Qing-yuan, CHEN Qiang, CHEN Yao, SU Ning, LIU Han-qing. Enhanced extra-long life fatigue resistance of a bimodal titanium alloy by laser shock peening [J]. International Journal of Fatigue, 2020, 141: 105868.
- [5] LI Jia-ning, LI Ji-shuai, QI Wen-jun, LIU Ke-gao. Characterization and mechanical properties of thick TC4 titanium alloy sheets welded joint by vacuum EBW [J]. Vacuum, 2019, 168: 108812.
- [6] FU Peng-fei, MAO Zhi-yong, WANG Ya-jun, ZUO Cong-jin, XU Hai-ying. Mechanical properties of Ti6.5Al2Zr1Mo1V titanium alloy with EBW under different temperatures [J]. Materials Science and Engineering A, 2014, 608: 199–206.
- [7] LONG Jian, ZHANG Lin-jie, ZHANG Liang-liang, WANG Xiang, ZHANG Gui-feng, ZHANG Jian-xun, NA S J. Effects of minor Zr addition on the microstructure and mechanical properties of laser welded joint of Al/SiC_p metal-matrix composite [J]. Journal of Manufacturing Processes, 2020, 49: 373–384.
- [8] LONG Jian, ZHANG Lin-jie, NING Jie, ZHANG Liang-liang, WANG Xiang, LI Sen, NA Suck-joo. Effects of post-weld heat treatment on microstructures and properties of laser welded joints of new high-strength Ti-55531 alloy [J]. Journal of Manufacturing Processes, 2021, 64: 1329–1335.
- [9] CHAMANFAR A, HUANG M F, PASANG T, TSUKAMOTO M, MISIOLEK W Z. Microstructure and mechanical properties of laser welded Ti–10V–2Fe–3Al (Ti1023) titanium alloy [J]. Journal of Materials Research and Technology, 2020, 9: 7721–7731.
- [10] FANG Nai-wen, GUO Er-jun, HUANG Rui-sheng, YIN Li-meng, CHEN Yong-sheng, ZENG Caiyou, CAO Hao, ZOU Ji-peng, XU Kai-xin. Effect of welding heat input on microstructure and properties of TC4 titanium alloy ultra-narrow gap welded joint by laser welding with filler wire [J]. Materials Research Express, 2021, 8: 016511–016522.
- [11] ZHANG Hai-bo, ZHANG Lin-jie, LIU Jiang-zhe, NING Jie, ZHANG Jian-xun, NA S J, ZHU Lei. Microstructures and performances of the butt joint of TA1/Q235B bimetallic sheet with addition of a Mo interlayer by using narrow gap laser welding with filler wire [J]. Journal of Materials Research and Technology, 2020, 9: 10498–10510.
- [12] SHI Hao, ZHANG Ke, XU Zheng-xi, HUANG Tian-yu, FAN Li-wen, BAO Wei-ning. Applying statistical models optimize the process of multi-pass narrow-gap laser welding with filler wire [J]. The International Journal of Advanced Manufacturing Technology, 2014, 75: 279–291.
- [13] YU Y C, YANG S L, YIN Y, WANG C M, HU X Y, MENG X X, YU S F. Multi-pass laser welding of thick plate with filler wire by using a narrow gap joint configuration [J]. Journal of Mechanical Science and Technology, 2013, 27: 2125–2131.
- [14] LONG Jian, ZHANG Lin-jie, NING Jie, MA Zheng-xion, ZANG Shun-lai. Zoning study on the fatigue crack propagation behaviors of a double-sided electron beam welded joint of TC4 titanium alloy with the thickness of 140 mm [J]. International Journal of Fatigue, 2021, 146: 106145.
- [15] FENG R C, RUI Z Y, ZUO Y, YAN C F, ZHANG G T. Influence of temperature on fatigue crack propagation in TiAl alloys [J]. Strength of Materials, 2014, 46: 417–421.
- [16] LONG Jian, ZHANG Lin-jie, ZHANG Qun-bing, WANG Wen-ke, ZHONG Jie, ZHANG Jian-xun. Microstructural characteristics and low cycle fatigue properties at 230 °C of different weld zone materials from a 100 mm thick dissimilar weld of ultra-supercritical rotor steel [J]. International Journal of Fatigue, 2020, 130: 105248.
- [17] XU Yuan-ming, ZHANG Shu-ming, HE Tian-peng, LIU Xin-ling, CHANG Xia-yuan. Prediction of low-cycle crack initiation life of powder superalloy FGH96 with inclusions based on damage mechanics [J]. Transactions of Nonferrous Metals Society of China, 2022, 32: 895–907.
- [18] HU Yong, YANG Xiao-kang, KANG Wen-jiang, DING Yu-tian, XU Jia-yu, ZHANG Hui-ying. Effect of Zr content on crack formation and mechanical properties of IN738LC processed by selective laser melting [J]. Transactions of Nonferrous Metals Society of China, 2021, 31: 1350–1362.
- [19] BEBER V C, SCHNEIDER B. Fatigue of structural adhesives under stress concentrations: Notch effect on fatigue strength, crack initiation and damage evolution [J]. International Journal of Fatigue, 2020, 140: 105824.
- [20] NANDAGOPAL R A, CHAI G B, NARASIMALU S. Influence of stress ratio and stress concentration on the fatigue behaviour of hygrothermal aged multidirectional CFRP composite laminate [J]. International Journal of Fatigue, 2020, 137: 1–12.

两种高能束焊 TC4 合金接头的低周疲劳性能比较

龙 健¹, 张林杰¹, 朱 磊¹, 张黎旭², 吴 军², 庄明祥³

1. 西安交通大学 材料力学行为国家重点实验室, 西安 710049;

2. 西安航天动力机械厂有限公司, 西安 710025;

3. 中航工业西安飞机工业(集团)有限责任公司, 西安 710089

摘 要: 比较 30 mm 厚 Ti6Al4V 钛合金真空电子束焊接和激光摆动填丝焊接头的低周疲劳性能。测试结果表明, 电子束焊接头的低周疲劳性能接近母材, 而激光填丝焊接头的低周疲劳性能明显不如电子束焊接头和母材。通过研究两个接头的母材、热影响区和焊缝区的显微硬度, 发现电子束焊接头的焊缝区显微硬度与母材的接近, 但均低于热影响区的显微硬度, 而激光填丝焊接头的焊缝区明显弱化。

关键词: Ti6Al4V 钛合金; 显微组织; 显微硬度; 低周疲劳

(Edited by Xiang-qun LI)